

Renormalization Treatment of IR and UV Cutoffs in Waveguide QED and Implications to Numerical Model Simulation

Romain Piron¹ and Akihito Soeda^{1, 2, 3}

¹*National Institute of Informatics, Chiyoda ku, Tokyo, Japan*

²*Department of Informatics, School of Multidisciplinary Sciences, SOKENDAI, Japan*

³*Department of Physics, Graduate School of Science, The University of Tokyo, Japan*

(Dated: January 23, 2026)

We present a non-perturbative, first-principles derivation of renormalization relations for waveguide-QED models, explicitly accounting for the infrared (IR) and ultraviolet (UV) cutoffs that are necessarily introduced in numerical simulations. By formulating the atomic dynamics in the time domain, we obtain explicit expressions linking the bare model parameters to the physically observable atomic frequency and decay rate, and verify their consistency with scattering theory. We further connect these results to standard Feynman diagrams, providing a transparent physical interpretation and ensuring the generality of the approach. Finally, we show how these renormalization relations can be used to parameterize simulations with a minimal frequency bandwidth, simultaneously preserving physical accuracy and reducing computational cost, thereby paving the way for efficient and reliable multi-photon light-matter simulations.

INTRODUCTION

Light-matter interactions are a cornerstone of modern quantum information science and constitute a fundamental resource for photonic quantum technologies. The initial proposal by Knill, Laflamme, and Milburn (KLM) [1] for photonic quantum computing demonstrated that universal quantum gates can, in principle, be realized using only linear optical elements supplemented by projective measurements based on photodetection, thereby inducing effective interactions between photons mediated by their coupling to material devices [1–3]. Similarly, distributed quantum architectures require entanglement generation between distant nodes [4–6], achieved via the interference of photons emitted by spatially separated matter qubits and implemented using linear optical setups with conditional detection [7–9]. Hence, acquiring a precise understanding of light–matter interactions, with the accuracy required for quantum information processing [10–12], is essential for guiding the design of quantum information processing architectures.

At a more elementary level, theoretical and numerical descriptions of light-matter interactions are commonly formulated within a Hamiltonian framework, in which the matter degrees of freedom are modeled using effective two-level systems (TLS) [13, 14]. Early numerical studies showed that TLS coupled to electromagnetic modes in cavities, as described by Jaynes-Cummings-type Hamiltonian [15, 16], already provide a powerful framework for simulating linear optical devices and protocols [17, 18].

However, recent research on light-matter interactions for quantum information processing has increasingly focused on nonlinear optics. Indeed, while the KLM scheme provides a scalable route toward photonic quantum computing using linear optical elements, the effective interactions it enables are measurement-induced and come at the cost of significant resource overhead [2]. This limitation has motivated extensive efforts to realize in-

trinsic photon-photon interactions using nonlinear optical platforms and light-matter interfaces [2, 19].

In this context, considerable attention has been devoted to *waveguide QED* setups. In such configurations, the matter systems—commonly referred to as atoms—are faithfully modeled as two-level systems (TLS) and are coupled to photons whose propagation is transversely confined to a region comparable to the atomic cross section [19]. A common theoretical description represents the propagating medium as a one-dimensional waveguide in which individual TLS are placed at fixed positions. A large body of theoretical work has studied this setting with a single TLS [19–30], while a variety of experimental platforms have demonstrated the feasibility of this approach [31–35]. These systems provide a promising route toward intrinsic photon-photon interactions mediated by strong light-matter coupling, potentially offering more practical architectures for photonic quantum computing compared with measurement-based schemes such as KLM [2].

The effective photon-photon interaction induced by the TLS renders the multi-photon regime analytically challenging: the resulting correlations make the *S*-matrix non-factorizable, motivating the development of reliable numerical simulation methods. In this context, it is essential to clearly identify the assumptions underlying the chosen theoretical framework. Several approaches based on wave-function methods [36, 37] or matrix-product states [38] have been developed, each relying on different representations of the photonic bath. Some aim for a first-principles description without approximations in the frequency domain, while others adopt effective representations inspired by the standard input-output formalism [26], in which frequency integrals are extended.

From a quantum field-theoretical perspective, coupling a discrete system to a continuum generally leads to frequency integrals that require proper regularization, giving rise to renormalization effects [39, 40], whereby physical observables are shifted away from their bare values.

Explicit control over the frequency-domain representation of the photonic bath is therefore essential for building reliable numerical simulations. Furthermore, these modeling choices are not merely of formal or conceptual significance but have practical experimental relevance. A paradigmatic example is the Lamb shift [41], in which atomic energy levels are modified by their interaction with the continuum of electromagnetic modes. Notably, even far off-resonant modes can contribute significantly to these shifts and thereby influence the system dynamics [42].

Furthermore, in numerical simulations of light-matter interactions, the photonic bath must be truncated so that frequency integrals have finite support, a requirement for computational tractability [38, 43]. In practice, this truncation amounts to introducing both infrared (IR) and ultraviolet (UV) cutoffs in the frequency domain. Intuitively, narrowing the frequency bandwidth reduces the effective size of the model and thereby improves computational efficiency. This reduction is directly reflected in the dimension of the finite Hilbert space used in the numerical representation [18]. From a computational standpoint, there is therefore a strong motivation to restrict the frequency window as much as possible. However, such truncations must be handled with care: as discussed above, physical observables can be sensitive to the treatment of the photonic continuum, including contributions from far off-resonant modes. Understanding and controlling both the representation of the photonic bath and the effects induced by frequency cutoffs is thus crucial for designing light-matter simulators that are simultaneously reliable and computationally efficient.

In this work, we present an end-to-end numerical simulation of a one-dimensional waveguide QED setup describing photon scattering from a central TLS, based on a first-principles wave-function approach with minimal assumptions on the frequency-domain description of the photonic bath. We place particular emphasis on the role of IR and UV cutoffs, providing a comprehensive and reproducible framework for reliable light-matter simulations. After introducing the model and numerical approach in Sec. I, we show in Sec. II that IR and UV cutoffs lead to observable renormalization effects by comparing numerical results with analytical predictions for single-photon scattering. We then derive explicit renormalization relations for the TLS transition frequency and decay rate in Sec. III, using an equation-of-motion approach that makes the role of the cutoffs transparent. In Sec. IV, we present a practical, renormalization-aware parameterization that enables accurate and computationally efficient simulations. Finally, Sec. V connects our approach to perturbative loop corrections, providing physical insight and indicating how these results extend to multi-photon scattering.

I. HAMILTONIAN AND NUMERICAL FRAMEWORK

This section defines the Hamiltonian of the system and the Runge-Kutta scheme used to simulate the resulting dynamics.

A. Hamiltonian description and discretization

We consider a standard waveguide QED setup in which a single atom, modeled as a two-level system (TLS) with transition frequency ω_0 and decay rate γ , is located at the origin $x = 0$ of a one-dimensional waveguide (see Fig. 1(a)). In the rotating-wave approximation (RWA) [16], the interaction between waveguide photons and the TLS is described, in units where $\hbar = 1$, by [19, 20, 25]:

$$H = \int_{-\infty}^{\infty} \frac{dk}{2\pi} \omega_k a^\dagger(k) a(k) + \omega_0 \sigma^+ \sigma^- + i \sqrt{\frac{\gamma}{2}} \int_{-\infty}^{\infty} \frac{dk}{2\pi} [a(k) \sigma^+ - \text{h.c.}] \quad (1)$$

The operators σ^+ and σ^- are the usual Pauli raising and lowering operators of the TLS defined as follows:

$$\begin{aligned} \sigma^+ &= |e\rangle \langle g|, \\ \sigma^- &= |g\rangle \langle e|, \end{aligned} \quad (2)$$

where $|g\rangle$ and $|e\rangle$ denote the ground and excited states of the TLS, respectively. The creation operator $a^\dagger(k)$ creates a photon with momentum k propagating in the waveguide, while the annihilation operator $a(k)$ annihilates it. These operators satisfy the canonical bosonic commutation relations:

$$\begin{aligned} [a(k), a(p)^\dagger] &= (2\pi) \delta(k - p), \\ [a(k), a(p)] &= [a(k)^\dagger, a(p)^\dagger] = 0. \end{aligned} \quad (3)$$

For later convenience, we explicitly decompose the Hamiltonian into its free and interaction parts, denoted by H_0 and V , respectively:

$$H_0 = \int_{-\infty}^{\infty} \frac{dk}{2\pi} \omega_k a^\dagger(k) a(k) + \omega_0 \sigma^+ \sigma^-, \quad (4a)$$

$$V = i \sqrt{\frac{\gamma}{2}} \int_{-\infty}^{\infty} \frac{dk}{2\pi} [a(k) \sigma^+ - \text{h.c.}] \quad (4b)$$

The dispersion relation ω_k depends on the properties of the waveguide. For theoretical treatments, it is commonly assumed to consist of two symmetric branches around $k = 0$. This allows one to linearize ω_k around a given frequency $\tilde{\omega}$ with corresponding momenta $\pm \tilde{k}$ [19]:

$$\begin{aligned} \omega_k &\approx \begin{cases} \tilde{\omega} + v_g(k - \tilde{k}) & \text{if } k > 0 \\ \tilde{\omega} - v_g(k + \tilde{k}) & \text{if } k < 0 \end{cases} \\ \text{where } v_g &= \left(\frac{\partial \omega_k}{\partial k} \right)_{\tilde{k}} = - \left(\frac{\partial \omega_k}{\partial k} \right)_{-\tilde{k}} \end{aligned} \quad (5)$$

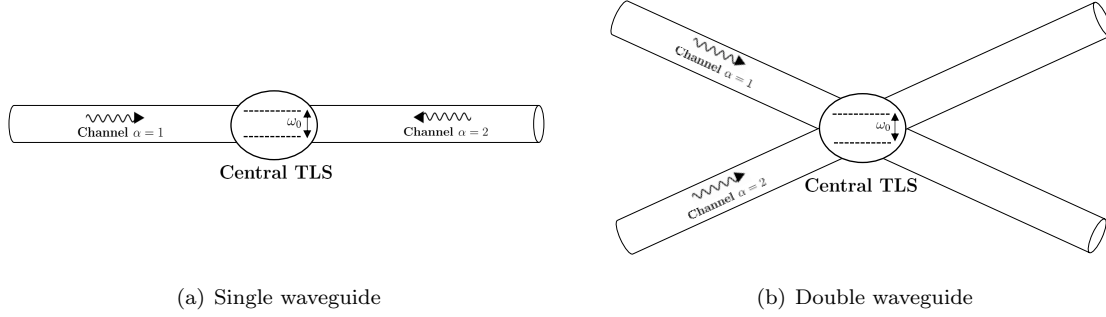


FIG. 1: Schematic representation of the waveguide QED setup under consideration. Panel (a) illustrates the case where the two channels correspond to right- and left-moving modes of a single waveguide, while panel (b) depicts the case of two distinct waveguides, each supporting unidirectional propagation.

Substituting the linearized dispersion relation into the free Hamiltonian and shifting the zero-point energy of each linearized branch by $\tilde{\omega} - v_g \tilde{k}$, we obtain:

$$H_0 = v_g \int_{k>0} \frac{dk}{2\pi} k a^\dagger(k) a(k) - v_g \int_{k<0} \frac{dk}{2\pi} k a^\dagger(k) a(k) + \omega_0 \sigma^+ \sigma^- \quad (6)$$

From this point on, it is convenient to perform the change of variable $k \rightarrow -k$ in the second integral [19], and to introduce a channel index α (as, for example, in Ref. [29]) to keep track of the branch of the dispersion relation. Concretely, we define the operators:

$$\begin{cases} a_1(k) = a(k) \\ a_2(k) = a(-k) \end{cases} \quad \text{for } k > 0 \quad (7)$$

where $\alpha = 1$ (resp. $\alpha = 2$) corresponds to the right-moving (resp. left-moving) branch of the dispersion relation. The Hamiltonian can then be expressed as an integral over positive momenta only:

$$H = \sum_{\alpha} \int_0^{\infty} \frac{dk}{2\pi} k a_{\alpha}^\dagger(k) a_{\alpha}(k) + \omega_0 \sigma^+ \sigma^- + i \sqrt{\frac{\gamma}{2}} \sum_{\alpha} \int_0^{\infty} \frac{dk}{2\pi} [a_{\alpha}(k) \sigma^+ - \text{h.c.}] \quad (8)$$

where, for simplicity, we set $v_g = 1$. The bosonic commutation relations are now given by:

$$\begin{aligned} [a_{\alpha}(k), a_{\beta}(p)^\dagger] &= (2\pi) \delta_{\alpha\beta} \delta(k-p), \\ [a_{\alpha}(k), a_{\beta}(p)] &= [a_{\alpha}(k)^\dagger, a_{\beta}(p)^\dagger] = 0. \end{aligned} \quad (9)$$

It is worth noting that the present description, although derived from a single-waveguide model, applies to more general geometrical setups. For instance, photons propagating unidirectionally—so-called chiral photons [27]—in two distinct waveguides coupled to the same two-level system, as illustrated in Fig. 1(b), lead to the same Hamiltonian.

In order to design a numerical simulation of this model, the Hamiltonian must be discretized appropriately. To this end, the propagation channels are taken to be finite, with length L , and periodic boundary conditions are imposed, leading to momentum quantization [17, 18]:

$$k_i = n_i \frac{2\pi}{L}, \quad n_i = 0, 1, 2, \dots, \quad (10)$$

together with the replacement [13]:

$$\int_0^{\infty} dk \rightarrow \frac{2\pi}{L} \sum_k \quad (11)$$

The discrete Hamiltonian then reads:

$$H = \sum_{\alpha, k} \omega_k a_{\alpha k}^\dagger a_{\alpha k} + \omega_0 \sigma^+ \sigma^- + i \sqrt{\frac{\gamma}{2L}} \sum_{\alpha, k} [a_{\alpha k} \sigma^+ - \text{h.c.}] \quad (12)$$

where we have introduced the discrete bosonic operators $a_{\alpha k} = a_{\alpha}(k)/\sqrt{L}$, which obey the discrete commutation relations:

$$\begin{aligned} [a_{\alpha k}, a_{\beta p}^\dagger] &= \delta_{\alpha\beta} \delta_{kp}, \\ [a_{\alpha k}, a_{\beta p}] &= [a_{\alpha k}^\dagger, a_{\beta p}^\dagger] = 0. \end{aligned} \quad (13)$$

With the Hamiltonian thus discretized, we now turn to the numerical scheme used to simulate the dynamics generated by this Hamiltonian.

B. Runge-Kutta based simulation

Following [17], it is convenient to work in the interaction picture, where states and operators are related to those in the Schrödinger picture via

$$|\psi_I(t)\rangle = e^{iH_0 t} |\psi_S(t)\rangle, \quad (14a)$$

$$\mathcal{O}_I(t) = e^{iH_0 t} \mathcal{O}_S e^{-iH_0 t}. \quad (14b)$$

In the interaction picture, the state evolves according to the Schrödinger equation:

$$i \partial_t |\psi_I(t)\rangle = V_I(t) |\psi_I(t)\rangle, \quad (15)$$

where the interaction Hamiltonian in the interaction picture takes the explicit form:

$$V_I(t) = i \sqrt{\frac{\gamma}{2L}} \sum_{\alpha,k} \left[e^{-i(\omega_k - \omega_0)t} a_{\alpha k} \sigma^+ - \text{h.c.} \right], \quad (16)$$

where we henceforth set $\omega_k = k$.

In this work, we use the fourth-order Runge-Kutta method suggested in [17] to numerically integrate the Schrödinger equation. The iterative scheme, detailed in Appendix A, produces a discrete sequence of states $|\psi_{I,n}\rangle$ that approximate the system's state at time steps $t_n = n\delta t$ over the simulation interval $[0, T]$. The index n ranges from 0 to N_{step} , where the time increment is defined as $\delta t = T/N_{\text{step}}$. Reducing the time step δt improves the accuracy of the system's evolution, but increases the computational cost since N_{step} must also be increased.

To access the physical observables of the model, one must expand the numerical states $|\psi_{I,n}\rangle$ in an appropriate basis in order to compute the associated probability amplitudes. A natural choice is the eigenbasis of the free Hamiltonian [17, 18], namely $|\alpha_1 k_1, \alpha_2 k_2, \dots, \sigma\rangle$, where $\alpha_i = 1, 2$ labels the channel in which the i -th photon propagates, k_i denotes its corresponding momentum, and $|\sigma\rangle = |g\rangle, |e\rangle$ specifies the atomic state.

This basis being infinite dimensional, it must be suitably truncated for numerical simulations. Moreover, keeping the basis as small as possible is essential for fast computation [18]. It is therefore natural to exploit all available symmetries of the Hamiltonian to minimize the number of free-basis vectors actually required. In particular, the absence of counter-rotating terms ensures conservation of the total number of excitations [16, 27]:

$$[H, N] = 0, \quad N = \sum_{\alpha,k} a_{\alpha k}^\dagger a_{\alpha k} + \sigma^+ \sigma^-. \quad (17)$$

Hence, with N fixed by the initial conditions, the basis can be restricted to the subspace containing exactly N excitations. Secondly, the set $\{0, 2\pi/L, 4\pi/L, \dots\}$ over which photon momenta take values is unbounded and must therefore be truncated. The choice of the truncation is, to the best of our knowledge, rarely discussed in the literature when implementing such numerical simulations. However, this issue deserves careful consideration, as we now argue.

C. Cutoff selection and computational cost

Fixing the frequency window is a crucial step in the design of fast numerical simulations of light-matter interaction systems [18, 38, 43], since it restricts the numerical Hilbert space to a finite and computationally

tractable size. Because the frequency space is naturally lower bounded, as $\omega_k > 0$, a minimal choice would be to introduce only an artificial ultraviolet (UV) cutoff. However, the Hamiltonian employed here is typically justified in the regime of weak photon-TLS detuning, where the RWA is valid [16, 17]. This suggests that a narrow frequency window around ω_0 may be sufficient.

To remain as general as possible, we instead introduce both an infrared (IR) and an ultraviolet (UV) cutoff, restricting the allowed momentum values to:

$$k_i \in [\Lambda_{\text{IR}}, \Lambda_{\text{UV}}]. \quad (18)$$

Accordingly, the integers n_i introduced in Eq. 10 satisfy:

$$\Lambda_{\text{IR}} \frac{L}{2\pi} \leq n_i \leq \Lambda_{\text{UV}} \frac{L}{2\pi}. \quad (19)$$

As a result, the dimension of the numerical Hilbert space restricted to a fixed number of excitations N is given by:

$$\dim(\mathcal{H}_{\text{num}}) = \left(2 \times \left\lfloor \frac{L}{2\pi} (\Lambda_{\text{UV}} - \Lambda_{\text{IR}}) \right\rfloor \right)^N + 1, \quad (20)$$

where the factor 2 accounts for the two photonic branches, and the additional degree of freedom corresponds to the atomic excitation $|0, e\rangle$. Although the dependence on the bandwidth $(\Lambda_{\text{UV}} - \Lambda_{\text{IR}})$ is only linear at the single-particle level, the tensor-product structure of the N -excitation sector induces a power-law growth of the Hilbert-space dimension with N . Moreover, each iteration of the Runge-Kutta propagation scheme requires $\mathcal{O}(\dim(\mathcal{H}_{\text{num}}))$ operations (see Appendix A). Consequently, even a moderate increase of the numerical bandwidth leads to a substantial rise in computational cost, severely limiting the range of accessible excitation numbers.

Although narrowing the frequency window is computationally appealing, it may also exclude physically relevant processes and compromise the validity of the model. In particular, the potential influence of off-resonant modes [42], as highlighted in the introduction, calls for a systematic assessment of the impact of both IR and UV cutoffs on physical observables. Therefore, the design of the present simulation requires a careful balance between computational efficiency and physical accuracy. In the next section, we address this issue through benchmark studies of single-photon scattering.

II. ASSESSING BANDWIDTH EFFECTS VIA SINGLE-PHOTON SCATTERING

Single-photon scattering off a TLS governed by the Hamiltonian H has been extensively studied in the literature [19–30], making it an ideal benchmark for assessing the physical accuracy of our numerical simulations. In this section, we use this setting to examine whether the simulator, for a given cutoff parameterization, yields accurate results.

A. Single-photon scattering matrix

The mathematical object encoding the scattering properties of the system is the S -operator [26, 27, 39]:

$$S = \mathcal{T} \exp \left(-i \int_{-\infty}^{+\infty} dt H_I(t) \right), \quad (21)$$

where \mathcal{T} denotes the time-ordering. Its matrix elements in the eigenbasis of the free Hamiltonian are denoted

$$\begin{aligned} S_{\alpha_1 k_1, \alpha_2 k_2, \dots, \sigma}^{\beta_1 p_1, \beta_2 p_2, \dots, \nu} \\ = \langle \beta_1 p_1, \beta_2 p_2, \dots, \nu | S | \alpha_1 k_1, \alpha_2 k_2, \dots, \sigma \rangle. \end{aligned} \quad (22)$$

As a brief aside, it is worth noting that these quantities do not always coincide with conventional S -matrix elements. Indeed, the latter are defined as overlaps between in- and out-states that are stationary under the *full* Hamiltonian [26, 39]. A free state with $|\sigma\rangle = |e\rangle$ cannot represent such an in- or out-state, since the atomic excitation becomes unstable once the interaction is turned on. Although evaluating matrix elements of the S -operator between free states with $|\sigma\rangle = |e\rangle$ is mathematically well defined [39], these quantities correspond to decay rates rather than to scattering amplitudes. In contrast, within the subspace where $|\sigma\rangle = |g\rangle$, the free states *can* correspond to stationary in- and out-states of the full Hamiltonian, and the corresponding matrix elements coincide with genuine S -matrix elements.

Single-photon scattering processes are well understood theoretically (see, e.g., [19–30]) and are described by the following S -matrix elements, whose derivation is commonly attributed to Ref. [23]:

$$S_{\beta p, g}^{\alpha k, g} = s_{\alpha\beta}(k) \delta(k - p), \quad (23)$$

The unitary matrix $s_{\alpha\beta}(k)$ can be written as [29]:

$$\begin{pmatrix} s_{11} & s_{12} \\ s_{21} & s_{22} \end{pmatrix} = \begin{pmatrix} t_k & r_k \\ -r_k & t_k \end{pmatrix}. \quad (24)$$

In the present work, we adopt the notation of Ref. [29], which is well suited to this standard waveguide-QED configuration. The reflection and transmission coefficients are given by:

$$r_k = -\frac{i\gamma/2}{(\omega_k - \omega_0) + i\gamma/2}, \quad t_k = \frac{\omega_k - \omega_0}{(\omega_k - \omega_0) + i\gamma/2}, \quad (25)$$

with $\omega_k = k$ in the present setup. From these relations, perfect reflection is expected at resonance, namely:

$$|r_{k_0}|^2 = 1, \quad |t_{k_0}|^2 = 0. \quad (26)$$

We will therefore perform preliminary numerical checks to assess which cutoff parameterizations enable the simulation to consistently reproduce this behavior. To this end, we first detail how these quantities are extracted from the simulation.

B. Numerical setup

The system containing initially a single photon, the numerical simulation can be restricted to the $N = 1$ sector of the free basis. Hence, the numerical states produced by the Runge-Kutta propagation read:

$$|\psi_{I,n}\rangle = \sum_{\alpha, k \in [\Lambda_{\text{IR}}, \Lambda_{\text{UV}}]} c_{\alpha k, n} |ak, g\rangle + b_n |0, e\rangle. \quad (27)$$

We initialize the photon as a Gaussian wave packet in the first propagation channel, centered at momentum k_p with a standard deviation Δ_k in momentum space. In position space, the packet is centered at x_0 , and the TLS is initially in its ground state. The corresponding superposition is:

$$|\psi_{I,0}\rangle = \sum_{\alpha, k \in [\Lambda_{\text{IR}}, \Lambda_{\text{UV}}]} c_{\alpha k, 0} |ak, g\rangle, \quad (28)$$

with coefficients [17, 18]:

$$c_{\alpha k, 0} \sim \delta_{\alpha 1} \exp \left[-\frac{(k - k_p)^2}{4\Delta_k^2} - ikx_0 \right], \quad (29)$$

up to a normalization factor, computed numerically as a function of Λ_{IR} and Λ_{UV} , to ensure proper normalization of the wave packet. Assuming that the time window $[0, T]$ is sufficiently large for the TLS to relax back to the ground state $|g\rangle$, the transmission probability of the photon can be identified as the probability of finding it in the same channel after the interaction, evaluated at the final step of the numerical simulation. Likewise, the reflection probability corresponds to finding the photon in the second propagation channel:

$$\mathcal{T} = \sum_{k \in [\Lambda_{\text{IR}}, \Lambda_{\text{UV}}]} |c_{1k, N_{\text{step}}}|^2, \quad (30a)$$

$$\mathcal{R} = \sum_{k \in [\Lambda_{\text{IR}}, \Lambda_{\text{UV}}]} |c_{2k, N_{\text{step}}}|^2. \quad (30b)$$

On the other hand, theoretical analyses such as Ref. [20] ensure that, in such setups, the reflection and transmission probabilities are related to the initial state's amplitudes via:

$$\mathcal{T}^{(\text{th})} = \sum_{k \in [\Lambda_{\text{IR}}, \Lambda_{\text{UV}}]} |t_k c_{1k, 0}|^2, \quad (31a)$$

$$\mathcal{R}^{(\text{th})} = \sum_{k \in [\Lambda_{\text{IR}}, \Lambda_{\text{UV}}]} |r_k c_{1k, 0}|^2. \quad (31b)$$

In the monochromatic limit, reached when $\Delta_k \ll \gamma$ [20], modes far from the central momentum k_p do not contribute significantly to these expressions. Consequently, the simulation can be regarded as accurate if it reproduces the expected transmission and reflection ampli-

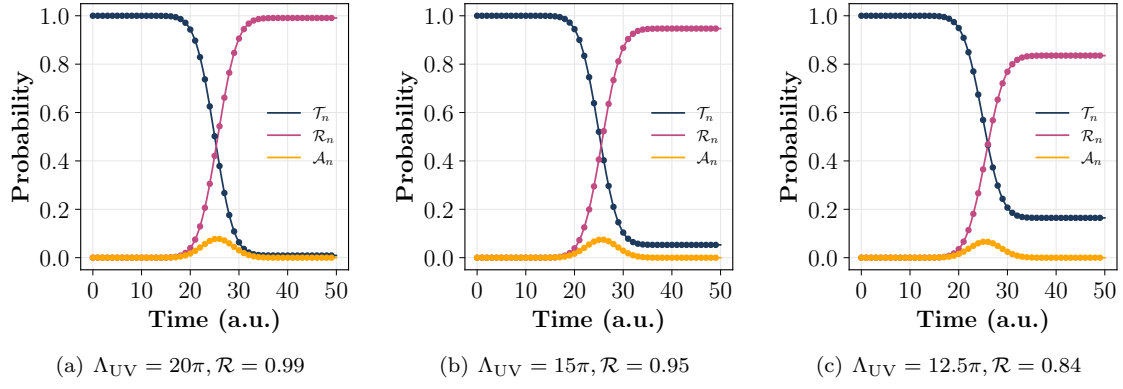


FIG. 2: Time evolution of the quantities \mathcal{R}_n , \mathcal{T}_n , and \mathcal{A}_n for the three different values of Λ_{UV} . Because the time step is small, the curves appear continuous, although they are obtained from consecutive discrete time steps.

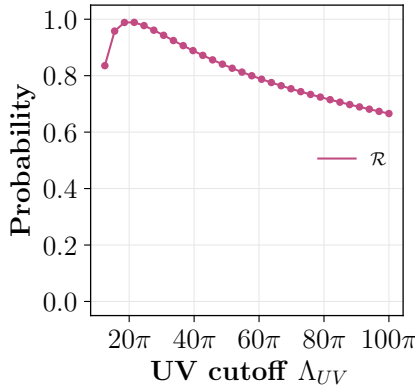


FIG. 3: Reflection probability at resonance $\omega_p = \omega_0$ as a function of the UV cutoff Λ_{UV} .

tudes derived from the S -matrix:

$$\begin{aligned} \mathcal{T} \xrightarrow[\Delta_k \ll \gamma]{} |t_{k_p}|^2 &= \frac{(\omega_p - \omega_0)^2}{(\omega_p - \omega_0)^2 + \gamma^2/4}, \\ \mathcal{R} \xrightarrow[\Delta_k \ll \gamma]{} |r_{k_p}|^2 &= \frac{\gamma^2/4}{(\omega_p - \omega_0)^2 + \gamma^2/4} \end{aligned} \quad (32)$$

We now turn to numerical checks where we compare the simulation results to these theoretical predictions.

C. Emergence of apparent deviations

For testing purposes, we set $L = 100$, $T = L/2 = 50$, $\omega_0 = 10\pi$, $\gamma = \pi$, and $\delta t = 0.01$, yielding a total number of time steps $N_{\text{step}} = T/\delta t = 5 \cdot 10^3$. This number of steps is deliberately taken large to avoid the accumulation of errors due to the finite precision of the numerical scheme.

We first consider scattering events in which the incoming photon is resonant with the atomic frequency ω_0 . In this case, perfect reflection is expected from Eq. 32. To validate this prediction, we perform three simulations

with progressively reduced UV cutoffs, thereby decreasing the numerical bandwidth. The IR cutoff is set to its minimal value, $\Lambda_{\text{IR}} = 0$. Specifically, we consider $\Lambda_{\text{UV}} = 2\omega_0$, $1.5\omega_0$, and $1.25\omega_0$. The initial wave packet is parameterized with $\omega_p = \omega_0 = 10\pi$, $x_0 = -L/4 = -25$ and $\Delta_k = 10^{-1}\gamma/2 = 0.05\pi$ to satisfy the resonance condition and ensure the monochromatic limit.

To track how the excitation is distributed within the system, we evaluate the following time-dependent quantities:

$$\mathcal{T}_n = \sum_{k \in [\Lambda_{\text{IR}}, \Lambda_{\text{UV}}]} |c_{1k,n}|^2, \quad (33a)$$

$$\mathcal{R}_n = \sum_{k \in [\Lambda_{\text{IR}}, \Lambda_{\text{UV}}]} |c_{2k,n}|^2, \quad (33b)$$

$$\mathcal{A}_n = |b_n|^2, \quad (33c)$$

which correspond to the probabilities of finding the excitation in the photonic modes of the first propagation channel, the second channel, or in the TLS, respectively. The reflection and transmission probabilities are then obtained at the final time step as $\mathcal{R} = \mathcal{R}_{N_{\text{step}}}$ and $\mathcal{T} = \mathcal{T}_{N_{\text{step}}}$.

The results in Fig. 2 confirm that perfect reflection is observed for $\Lambda_{\text{UV}} = 2\omega_0 = 20\pi$ (Fig. 2(a)), but they also show that this effect depends strongly on the UV cutoff. Decreasing the cutoff decreases the reflection probability \mathcal{R} . Moreover, the trends in Figs. 2(b) and 2(c) indicate that, in all cases, the atom has sufficient time to relax. Thus, the deviation does not originate from an unusual distribution of excitation within the system, but rather reflects an apparent shift in the physical atomic frequency away from ω_0 .

One might therefore conclude that reducing the UV cutoff below $\Lambda_{\text{UV}} = 2\omega_0 = 20\pi$ causes the simulation to miss relevant physical processes. A natural consistency check is to verify that increasing the UV cutoff beyond this value does not alter the expected perfect-reflection

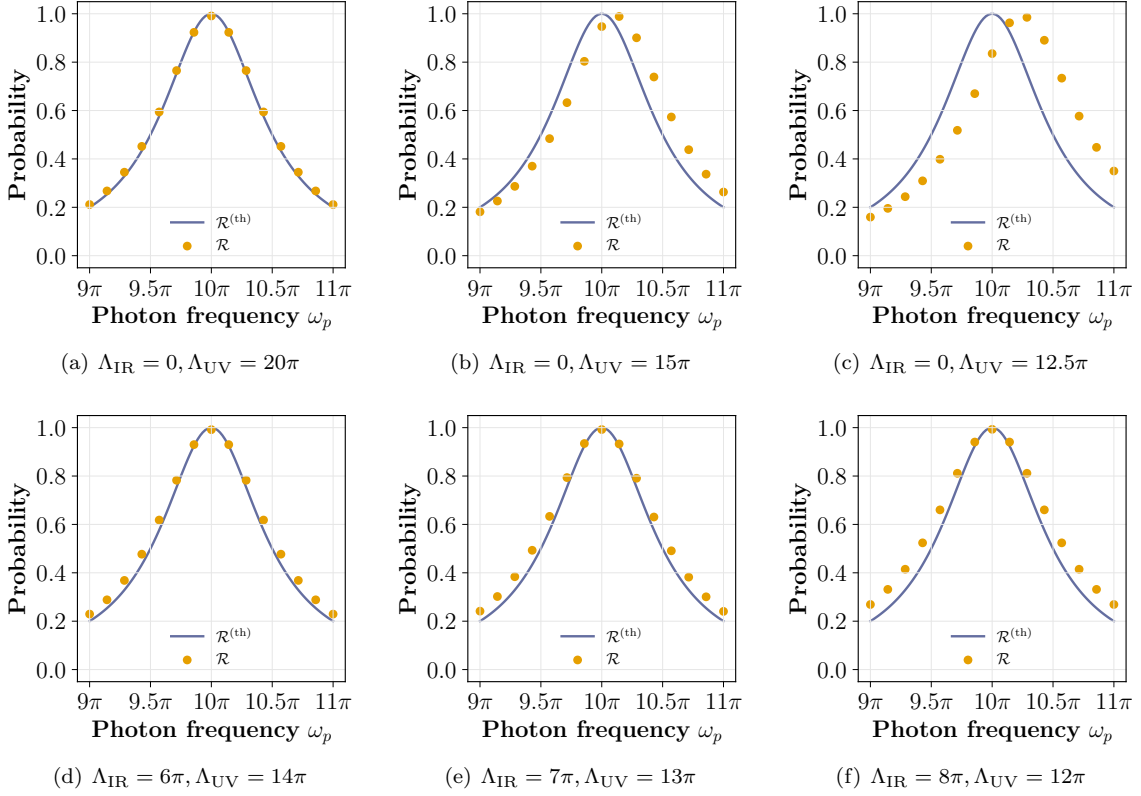


FIG. 4: Comparison between the numerically obtained reflection coefficient \mathcal{R} and the prediction $\mathcal{R}^{(\text{th})}$ across various frequency windows.

behavior. Surprisingly, this is not the case. As shown in Fig. 3, the correct theoretical prediction is recovered only for $\Lambda_{\text{UV}} = 2\omega_0$, while any deviation from this value leads to a breakdown of perfect reflection. Moreover, no clear convergence of the reflection probability at resonance is observed as the UV cutoff is increased. This unexpected sensitivity to the frequency truncation suggests that the physical predictions of the model depend on the numerical cutoff, which is unsatisfactory since the latter should remain a purely numerical artifact. Clarifying the origin of this behavior is one of the main goals of the present work. To gain further insight on the origin of this behavior, we now examine the behavior of \mathcal{R} as functions of ω_p for different choices of frequency windows.

D. Impact of IR and UV cutoffs

For the following simulations, we retain the parameters $L = 100$, $T = L/2 = 50$, $\omega_0 = 10\pi$, $\gamma = \pi$, and $\delta t = 0.01$. The system is again initialized with a Gaussian wave packet centered at $x_0 = -L/4 = -25$, in the monochromatic limit achieved through $\Delta_k = 10^{-1}\gamma/2 = 0.05\pi$. To examine the ω_p dependence of the reflection coefficient \mathcal{R} , we perform a series of scattering experiments for a fixed frequency window, using several values of ω_p sampled

within the interval $[\omega_0 - \gamma, \omega_0 + \gamma]$. The theoretical prediction in the monochromatic limit, $\mathcal{R}^{(\text{th})}(\omega_p) = |r_{k_p}|^2$, is shown as a benchmark.

We first compare the trends of \mathcal{R} and $\mathcal{R}^{(\text{th})}$ using the same frequency windows as in the previous testbed, namely $[\Lambda_{\text{IR}}, \Lambda_{\text{UV}}] = [0, 20\pi]$, $[0, 15\pi]$, and $[0, 12.5\pi]$. The corresponding results are shown in Figs. 4(a), 4(b), and 4(c), respectively. The overall agreement in the shapes of the curves strongly indicates that the previously observed deviations arise from a shift in the physical atomic frequency. Nevertheless, we observe that the match remains quite accurate for $\Lambda_{\text{UV}} = 20\pi$ (Fig. 4(a)). In this case, the frequency $\omega_0 = 10\pi$ lies exactly at the center of the numerical frequency window, which may explain why the physical frequency coincidentally aligns with ω_0 .

This motivates further tests in which we repeat the same type of experiment using frequency windows centered around ω_0 . The results shown in Figs. 4(d), 4(e), and 4(f) correspond to three such windows, namely $[\Lambda_{\text{IR}}, \Lambda_{\text{UV}}] = [6\pi, 14\pi]$, $[7\pi, 13\pi]$, and $[8\pi, 12\pi]$. In all cases, the location of the peak is accurately predicted by $\mathcal{R}^{(\text{th})}$, indicating that centering the numerical frequency window ω_0 makes it effectively coincide with the physical frequency. However, the width of the numerical data increases as the window becomes narrower. This ob-

servation suggests that, when varying the width of the frequency window, the parameter γ does not match the physical decay rate governing the scattering dynamics.

Our numerical simulations show that, in the presence of IR and UV cutoffs, the parameters ω_0 and γ , although commonly interpreted as the atomic transition frequency and decay rate [20, 22–30], do not generally coincide with the corresponding physical observables. From a renormalization perspective familiar from quantum field theory [39, 40], such behavior is expected in models involving a continuum of modes, where interactions generically shift observable quantities away from their nominal values. In the following, we will refer to these model-defined parameters ω_0 and γ as *bare parameters*, in contrast to the corresponding physical (renormalized) quantities, denoted ω_A and Γ .

While interaction-induced frequency shifts are sometimes acknowledged (see, e.g., Appendix A of Ref. [21] or Ref. [19]), they are often assumed for simplicity to be implicitly absorbed into the definition of ω_0 , or not discussed explicitly. As we will discuss further, this practice is closely tied to the choice of frequency-range extension mentioned in the introduction. In contrast, within the present first-principles description, renormalization effects naturally arise, making it necessary to explicitly relate the bare parameters of the model ω_0 and γ to the corresponding physical observables. This motivates a detailed characterization of the mapping between bare parameters and measurable quantities.

The results presented below suggest that the expressions in Eq. (25) correctly capture the functional form of the single-photon scattering amplitudes. It is therefore natural to expect that these amplitudes should ultimately be expressed in terms of the physical parameters rather than the bare ones. This leads us to consider the parametrization:

$$t_k^{(\text{phys})} = \frac{\omega_k - \omega_A}{(\omega_k - \omega_A) + i\Gamma/2}, \quad (34a)$$

$$r_k^{(\text{phys})} = -\frac{i\Gamma/2}{(\omega_k - \omega_A) + i\Gamma/2}, \quad (34b)$$

with:

$$\omega_A \neq \omega_0, \quad \Gamma \neq \gamma. \quad (35)$$

In the remainder of this paper, we derive the physical parameters ω_A and Γ from the underlying Hamiltonian in order to properly recalibrate the scattering description. Beyond this theoretical consistency, it is important to emphasize that experimental measurements directly access the physical parameters ω_A and Γ , while the bare quantities ω_0 and γ entering the Hamiltonian are not observable [39]. As a result, establishing a clear relation between bare and physical parameters is essential for both the interpretation of numerical simulations and any quantitative comparison with laboratory experiment.

III. FINITE IR AND UV INDUCED RENORMALIZATION

In this section, we present a theoretical derivation of the renormalization induced by the finite frequency bandwidth employed in the numerical simulations, together with a consistency check against the data analyzed previously. This derivation serves as the foundation for proposing a renormalization-aware parameterization of the simulation.

A. Decay of the atom: equations of motion

To relate the bare parameters to their physical counterparts, a consistency condition must be imposed. Since the renormalization concerns solely the parameters of the TLS, we fix these parameters by matching a TLS observable. Specifically, we consider the decay amplitude of the excited state into the cavity modes. Accordingly, when the atom is initially excited, the amplitude of the atomic state $|0, e\rangle$ evolves in the Schrödinger picture as:

$$b_S(t) = \exp\left(-i\omega_A t - \frac{\Gamma}{2}t\right). \quad (36)$$

Let us then assume that the system is initialized in $|0, e\rangle$. The conservation of the excitations number ensures that, at time t , the system's state can be expanded as:

$$|\psi_I(t)\rangle = \sum_{\alpha} \int_0^{\infty} \frac{dk}{2\pi} c_{\alpha k}(t) |\alpha k, g\rangle + b(t) |0, e\rangle. \quad (37)$$

Plugging this state into the Schrödinger's equation in the interaction picture yields the set of coupled equations:

$$\frac{dc_{\alpha k}}{dt} = -\sqrt{\frac{\gamma}{2}} e^{i(\omega_k - \omega_0)t} b(t) \quad (38a)$$

$$\frac{db}{dt} = \sqrt{\frac{\gamma}{2}} \sum_{\alpha} \int_0^{\infty} \frac{dk}{2\pi} e^{-i(\omega_k - \omega_0)t} c_{\alpha k}(t) \quad (38b)$$

Using $\omega_k = k$, the integration can be rewritten over $\omega \in [0, \infty)$. Since $c_{\alpha k}(0) = 0$, one can integrate the first equation and substitute the result into the second [13], yielding the following equation of motion for the atomic coefficient:

$$\frac{db}{dt} = \int_0^t d\tau K(\tau) b(t - \tau), \quad (39)$$

where $K(\tau) = -\frac{\gamma}{2\pi} \int_0^{\infty} d\omega e^{-i(\omega - \omega_0)\tau}$.

Following existing theoretical approaches that explicitly treat this equation of motion [21, 42], we introduced the kernel $K(\tau)$. Solving this equation of motion then allows us to extract the physical parameters ω_A and Γ . We now discuss how the kernel is typically treated and why, in the present setup, renormalization effects are expected to arise.

B. Atomic kernel with finite bandwidth

When the frequency domain is taken to be unbounded, the kernel K is broad in frequency space [21]. As a result, $K(\tau)$ is strongly peaked around $\tau = 0$, justifying the Markov approximation $b(t - \tau) \approx b(t)$ in the equation of motion. This leads to the simplified form [21, 42]:

$$\frac{db}{dt} = b(t) \left(\int_0^t d\tau K(\tau) \right). \quad (40)$$

In the numerical simulation, however, the introduction of hard cutoffs Λ_{IR} and Λ_{UV} modifies this picture. While the kernel $K(\tau)$ remains peaked near $\tau = 0$, its width is no longer negligible compared to the timescale over which $b(t)$ varies, potentially invalidating the Markov approximation. Nonetheless, providing the frequency window is not too narrow, one can still expect the kernel's contribution to take the form of a "delta function plus corrections," motivating a Taylor expansion of $b(t - \tau)$ around $\tau = 0$ and leading to the following series expansion of the equation of motion:

$$\frac{db}{dt} = \sum_{n \geq 0} \left(\frac{(-1)^n}{n!} \int_0^t \tau^n K(\tau) d\tau \right) \frac{d^n b}{dt^n}(t) \quad (41)$$

Let us denote by α_n the coefficient multiplying the n th-order time derivative of $b(t)$. Assuming that $K(\tau)$ is sufficiently peaked around $\tau = 0$, the time integral may be extended to the full domain $\tau > 0$. The coefficients then read:

$$\alpha_n = \frac{(-1)^{n+1}}{n!} \frac{\gamma}{2\pi} \int_0^\infty d\tau \int_{\Lambda_{\text{IR}}}^{\Lambda_{\text{UV}}} d\omega \tau^n e^{-i(\omega - \omega_0)\tau}, \quad (42)$$

$$\begin{cases} \omega_A &= \omega_0 - \frac{\gamma}{2\pi} f(\omega_0, \gamma) \log\left(\frac{\Lambda_{\text{UV}} - \omega_0}{\omega_0 - \Lambda_{\text{IR}}}\right), \\ \Gamma &= \gamma f(\omega_0, \gamma), \end{cases} \quad \text{with} \quad f(\omega_0, \gamma) = \left(1 - \frac{1}{\pi} \frac{\gamma}{H(\omega_0 - \Lambda_{\text{IR}}, \Lambda_{\text{UV}} - \omega_0)}\right)^{-1}, \quad (46)$$

where we used the following definition of the harmonic mean:

$$H(\omega_0 - \Lambda_{\text{IR}}, \Lambda_{\text{UV}} - \omega_0) = \left(\frac{1}{2} \left(\frac{1}{\omega_0 - \Lambda_{\text{IR}}} + \frac{1}{\Lambda_{\text{UV}} - \omega_0} \right) \right)^{-1} \quad (47)$$

This constitutes the main result of this paper. A few consistency checks can be mentioned:

- (i) First, one can observe that when the bare frequency lies at the center of the frequency window, i.e., when $\omega_0 - \Lambda_{\text{IR}} = \Lambda_{\text{UV}} - \omega_0$, the physical frequency

where the frequency integration limits have been made explicit. Strictly speaking, the τ -integral does not converge in the usual sense. However, it can be assigned a well-defined value by interpreting the integrand in the sense of distributions. A detailed analysis of these coefficients, provided in Appendix B, shows that they scale with n as:

$$\alpha_n = x_n \frac{\gamma}{(\omega_0 - \Lambda_{\text{IR}})^n} + y_n \frac{\gamma}{(\Lambda_{\text{UV}} - \omega_0)^n}, \quad n \geq 1, \quad (43)$$

where x_n and y_n are numerical coefficients. This behavior indicates that, as long as ω_0 lies sufficiently far from the cutoffs, higher-order terms can be safely neglected. We use this scaling to simplify and solve the equation of motion under this assumption.

C. Deduction of the physical parameters

Assuming that terms with $n \geq 2$ can be safely neglected, the equation of motion for the atomic coefficient in the interaction picture reads:

$$\frac{db}{dt} = (1 - \alpha_1)^{-1} \alpha_0 b(t). \quad (44)$$

With the initial condition $b(0) = 1$, the solution in the Schrödinger picture is then:

$$b_S(t) = \exp(-i\omega_0 t + (1 - \alpha_1)^{-1} \alpha_0 t), \quad (45)$$

The explicit computation of α_0 and α_1 , carried out in Appendix B, allows us to extract the physical parameters according to our initial prescription. One finally obtains:

coincides with the bare one. This is fully consistent with the behavior noted earlier (see Fig 4(a), 4(d), 4(e), 4(f)).

- (ii) The prefactor f is positive if and only if:

$$\gamma < \pi H(\omega_0 - \Lambda_{\text{IR}}, \Lambda_{\text{UV}} - \omega_0), \quad (48)$$

which naturally restricts the region over which the bare parameters can be chosen. Indeed, violating this condition would yield a negative physical decay rate, an unphysical result. This constraint is consistent with our assumption that the coefficients α_n with $n \geq 2$ can be neglected, since for a given bare

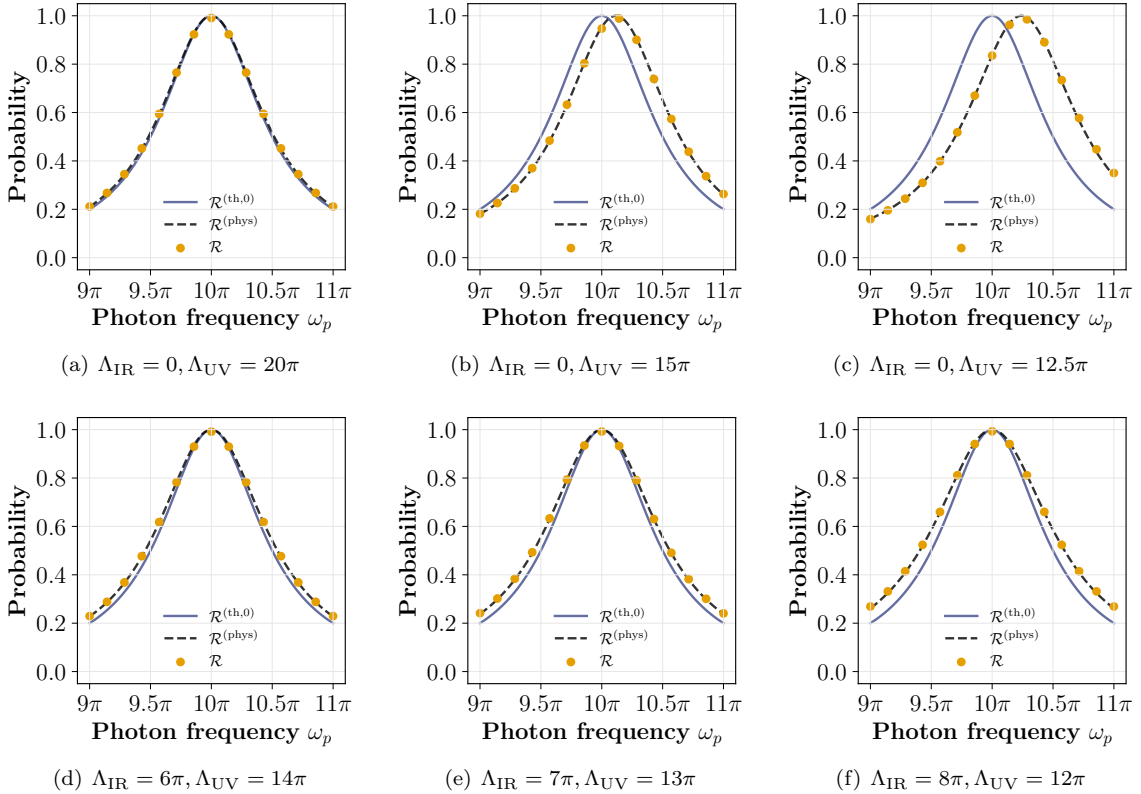


FIG. 5: Comparison between the numerically obtained reflection coefficient \mathcal{R} and the adjusted prediction $\mathcal{R}^{(\text{phys})}$ derived from the physical parameters, evaluated across different frequency windows. The bare prediction $\mathcal{R}^{(0)}$ is shown for reference.

decay rate γ , the bare frequency ω_0 must lie sufficiently far from both the IR and UV cutoffs.

- (iii) Moreover, when $\gamma \ll \pi H(\omega_0 - \omega_{\text{IR}}, \omega_{\text{UV}} - \omega_0)$, the prefactor approaches unity, causing the renormalization of the decay rate to vanish. This behavior is consistent with the results shown in Figs. 4(d), 4(e), 4(f), where the physical decay rate is observed to shift as the bandwidth is reduced.

In particular, point (i) deserves further attention, as it can be directly connected to existing works. The logarithmic contribution appearing in our results corresponds precisely to the usual *Lamb shift* [41, 44], which has been acknowledged in the present waveguide QED context, for instance in Appendix A of Ref. [21] or in Ref [19]. In our formulation, this contribution arises solely from the imaginary part of α_0 , while α_1 is purely real (see Appendix B). Interestingly, such frequency shifts are rarely discussed explicitly in earlier waveguide-QED treatments [20, 22–30]. This can be traced back to the common practice of extending frequency integrals to $\omega \in (-\infty, +\infty)$, a procedure often justified within the Weisskopf–Wigner framework [13]. While convenient, this extension renders the Hamiltonian unbounded and should therefore be understood as an effective description. At the same

time, it eliminates principal-value contributions in the frequency integrals, such as those explicitly appearing in Appendix B, thereby suppressing any renormalization effects. Within the present approach, this limit can be formally recovered by choosing the cutoffs $\Lambda_{\text{UV}} = x + \Omega$ and $\Lambda_{\text{IR}} = y - \Omega$ (with x and y arbitrary constants), and subsequently taking $\Omega \rightarrow +\infty$, in which case one finds $\omega_0 = \omega_A$ and $\gamma = \Gamma$. The framework introduced here thus provides a controlled renormalization of both the atomic frequency and the decay rate, thereby generalizing the standard Lamb-shift correction by consistently accounting for IR and UV cutoffs.

Let us now revisit the data generated in the numerical experiments shown in Fig. 4 and compare it with the deviations derived above. To this end, we denote by $\mathcal{R}^{(\text{phys})}$ the theoretical prediction given by Eq. 32, evaluated using the physical parameters ω_A and Γ . The previously used benchmark curve is now denoted $\mathcal{R}^{(\text{th},0)}$ to emphasize its dependence on the bare parameters. The results shown in Fig. 5 indicate that the dynamical response of the system is indeed governed by the physical parameters ω_A and Γ , as the numerical data are accurately captured by the prediction $\mathcal{R}^{(\text{phys})}$.

Several theoretical questions nevertheless remain. In particular, one may ask why the decay of the TLS

into the waveguide modes provides sufficient information to correct scattering predictions, and whether similar renormalization effects persist in the multiphoton regime. These issues are addressed in Sec. V, where the present approach is connected to Green's functions and Feynman diagrams within a perturbative framework. Before turning to this analysis, we first present an end-to-end, renormalization-aware parameterization that enables a substantial reduction of the computational cost while preserving physical accuracy.

IV. AN END-TO-END COMPUTATIONALLY EFFICIENT PARAMETERIZATION

The results presented in the previous section have important practical implications for the design of accurate waveguide-QED simulators. Laboratory measurements provide access only to physical parameters, whereas the bare ones are purely model-defined and not directly observable [39, 40]. Yet, numerical simulations of complex light-matter Hamiltonians are ultimately intended to predict measurable quantities. Consequently, when implementing a simulator, the input parameters should be the physical ones rather than the bare ones. This requirement implies that the renormalization relations must be *inverted* in order to determine the bare parameters to be supplied to the numerical model. This point therefore deserves a dedicated discussion, in which we outline a general prescription for the parameterization of such simulations.

A. Prescription for renormalization-consistent parameterization

Tuning the bare parameters to match the target physical values renders all predicted observables independent of the IR and UV cutoffs, which is the essential requirement in the design of such simulations. At the same time, this procedure highlights an apparent redundancy: starting from the two physical inputs ω_A and Γ , one must specify four numerical parameters, namely Λ_{IR} , Λ_{UV} , ω_0 , and γ , where Λ_{IR} and Λ_{UV} are scheme-dependent cut-offs introduced purely for numerical convenience. Hence, additional physical input is required to construct a consistent and unambiguous end-to-end parameterization of the simulator.

Since the present Hamiltonian is typically valid in the weak-detuning regime [16], a natural starting point is to introduce a frequency window centered on the *physical frequency*:

$$[\Lambda_{\text{IR}}, \Lambda_{\text{UV}}] = [\omega_A - \Lambda, \omega_A + \Lambda], \quad \Lambda > 0. \quad (49)$$

With this choice, setting $\omega_0 = \omega_A$ provides a trivial solution to the relation between the physical and bare frequencies, corresponding to a frequency window centered

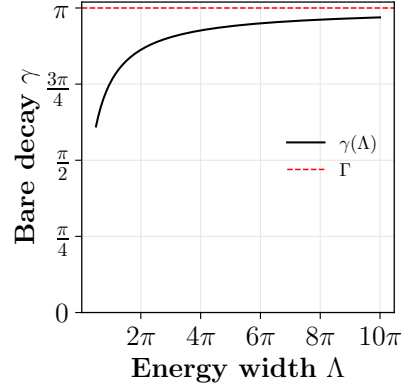


FIG. 6: Variation of the bare decay rate γ as a function of the energy width Λ of the frequency window centered around the physical atomic frequency $\omega_A = 10\pi$, for a fixed physical decay rate $\Gamma = \pi$. The dashed line indicates the value of Γ for reference.

on the bare atomic transition. The bare decay rate is then deduced from Eq. 46 as:

$$\gamma = \frac{\Gamma}{1 + \Gamma/(\pi\Lambda)}. \quad (50)$$

This relation automatically satisfies the positivity condition $f(\omega_0, \gamma) > 0$, which in this case reduces to:

$$f(\omega_0, \gamma) > 0 \iff \frac{\Gamma}{1 + \Gamma/(\pi\Lambda)} < \pi\Lambda, \quad (51)$$

which is always satisfied for $\Gamma, \Lambda > 0$. This has a practical implication: the frequency window may be chosen arbitrarily narrow around ω_A , to capture only the physically relevant part of the spectrum (e.g. atomic and photon frequencies in scattering experiments), provided that the bare decay rate γ is adjusted accordingly.

For concreteness, fixing the physical parameters to $\omega_A = 10\pi$ and $\Gamma = \pi$, Fig. 6 shows the dependence of the bare decay rate $\gamma(\Lambda)$ on the bandwidth Λ , with the physical value Γ indicated for reference. Notably, $\gamma(\Lambda)$ never coincides with Γ , underscoring the necessity of the renormalization considerations discussed throughout this work. Moreover, the deviation becomes increasingly pronounced as Λ is reduced, precisely in the regime of greatest interest for improving the computational efficiency of the simulations. We now argue that this renormalization-aware parameterization indeed enhances the efficiency of the simulations as Λ is decreased.

B. Computational gain

Adjusting the bare decay rate according to the renormalization prescription allows the simulation bandwidth to be safely reduced, provided that all relevant frequencies remain within the window. We assess this gain in efficiency by simulating single-photon scattering using the

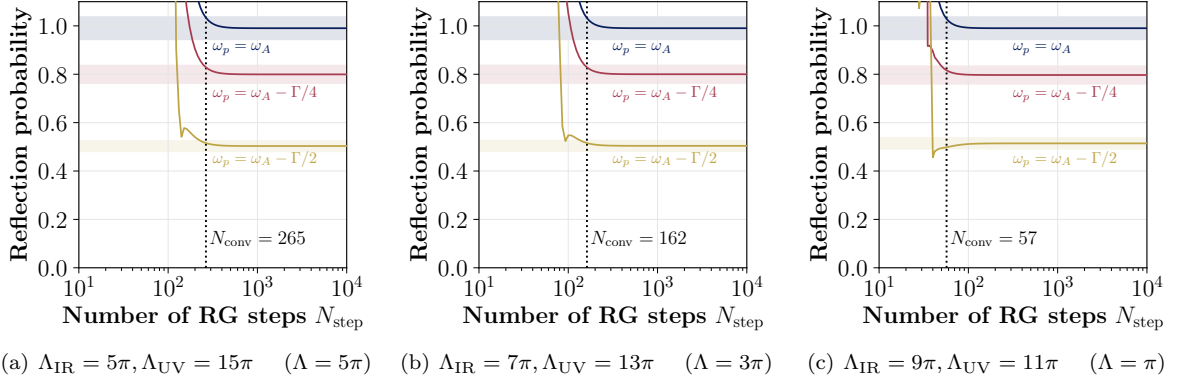


FIG. 7: Prediction of the reflection coefficient \mathcal{R} for three different photon frequencies ω_p against the number of time steps N_{step} , using the renormalization-consistent parameterization with different values of Λ . The dashed lines indicate the minimal number of steps required for convergence.

renormalization-consistent parameterization introduced above, and by examining the convergence of the reflection coefficient \mathcal{R} as a function of the number of Runge-Kutta time steps N_{step} for different bandwidths Λ .

To test the robustness of our approach, we first prepare the atom with bare parameters adjusted according to the prescription detailed above, keeping the physical values fixed at $\omega_A = 10\pi$ and $\Gamma = \pi$, and considering three different frequency bandwidths: $\Lambda = 5\pi, 3\pi, \pi$. For each bandwidth, we then perform three independent single-photon scattering simulations, using monochromatic incoming photons with frequencies $\omega_p = \omega_A$, $\omega_A - \Gamma/4$, and $\omega_A - \Gamma/2$, in order to probe different regions of the frequency window. The initial state is a Gaussian wave packet centered at $x_0 = -L/4$, with a width of $\Delta_k = 0.05\pi$, and we vary the time step to study convergence. Finally, for each bandwidth, we assess convergence by checking whether the reflection probability \mathcal{R} from the three independent experiments lies within 5% of the theoretical prediction $\mathcal{R}^{(\text{phys})}$.

The results of the simulations are shown in Fig. 7. For each bandwidth Λ , the three independent experiments all enter the 5% confidence region around the theoretical prediction $\mathcal{R}^{(\text{phys})}$ —indicated by the colored region along the y -axis—and converge as N_{step} is increased. This demonstrates the internal consistency of the model and shows that convergence is achieved independently of the bandwidth Λ .

Interestingly, the number of RG time steps required for convergence decreases as Λ is reduced. Since the total time window is kept fixed ($T = L/2 = 50$), this indicates that a narrower frequency window allows for larger time steps δt . Moreover, decreasing Λ reduces the dimension of the numerical Hilbert space, thereby lowering the computational cost of each Runge-Kutta propagation step (see Appendix A). For these two reasons, the overall computational cost can be substantially reduced by narrowing the frequency window while consistently renormalizing the bare parameters.

In summary, the parameterization we prescribe allows one to reduce the numerical bandwidth, thereby lowering the computational cost of the simulation, while ensuring that all physical predictions remain accurate. The complete parameterization proceeds as follows:

- (i) Choose Λ as small as possible such that the set of relevant frequencies $\{\omega_i\}_i$ (e.g. the incoming photon frequency ω_p) satisfies $\{\omega_i\}_i \subset [\omega_A - \Lambda, \omega_A + \Lambda]$.
- (ii) Set $\Lambda_{\text{IR}} = \omega_A - \Lambda$ and $\Lambda_{\text{UV}} = \omega_A + \Lambda$.
- (iii) Fix the bare frequency to $\omega_0 = \omega_A$.
- (iv) Fix the bare decay rate according to:

$$\gamma = \frac{\Gamma}{1 + \Gamma/(\pi\Lambda)}.$$

We emphasize that this prescription is not unique. In particular, the frequency window may be further reduced if physical considerations justify it, for instance when the set of relevant frequencies lies entirely below ω_A , so that higher energies need not be resolved. However, when restricting the window to only lower (or only higher) energies relative to ω_A , the inversion of the renormalization relations is no longer guaranteed to be straightforward. In such cases, one must explicitly verify that the chosen frequency window admits a consistent solution for the bare parameters. Hence, the proposed parameterization achieves a balance between conceptual simplicity and computational efficiency.

We now turn to a perturbative analysis that connects the present non-perturbative derivation of the physical parameters to the standard Green's function formalism in scattering theory, while also providing a natural extension to the multi-photon regime.

V. PERTURBATIVE ANALYSIS AND MULTI-PHOTON EXTENSION

Although our expressions for Γ and ω_A are non-perturbative, i.e., not truncated in powers of the coupling parameter $\gamma^{1/2}$, a perturbative analysis of the scattering amplitudes provides valuable physical insight into the structure of the corrections we computed and their impact on photon-scattering dynamics. Moreover, the formalism employed in this section has also been studied in the present waveguide-QED setup [27, 28, 30, 35, 45], allowing these corrections to be naturally extended to the multi-photon scattering regime.

A. Green's operator and single-photon scattering

First of all, let us argue that our definition of the physical parameters ω_A and Γ is consistently related to the usual approach in scattering theory, where physical parameters are associated with the poles of Green functions [39]. Assuming that the atom is initially excited at time t_0 , the atomic coefficient $b(t)$ can be formally written as:

$$b(t) = \langle 0, e | \psi(t) \rangle = \langle 0, e | \exp[-iH(t - t_0)] | 0, e \rangle. \quad (52)$$

Hence, its Fourier transform can be expressed as:

$$\begin{aligned} b(\omega) &= \int_{t_0}^{\infty} dt e^{i\omega t} b(t) \\ &= e^{i\omega t_0} \left\langle 0, e \left| \int_0^{\infty} dt e^{i(\omega - H)t} \right| 0, e \right\rangle. \end{aligned} \quad (53)$$

By introducing the causal prescription $\omega \rightarrow \omega + i\varepsilon$ [24] to ensure convergence of the time integral, one obtains:

$$b(\omega) = -i e^{i\omega t_0} \langle 0, e | G(\omega) | 0, e \rangle, \quad (54)$$

where we have introduced the Green operator [27, 30]:

$$G(\omega) = \frac{1}{\omega - H + i\varepsilon}. \quad (55)$$

Up to a phase factor depending on the initial excitation time, the momentum representation of the atomic coefficient therefore corresponds exactly to the matrix element $G_{0,e}^{0,e}(\omega)$ of the Green operator, that is, the atomic retarded Green function.

On the other hand, using the expression of the atomic amplitude in terms of the physical parameters, we also obtain:

$$\begin{aligned} b(\omega) &= e^{i\omega t_0} \int_0^{\infty} dt \exp \left[i \left(\omega - \omega_A + i \frac{\Gamma}{2} + i\varepsilon \right) t \right] \\ &= -i e^{i\omega t_0} \frac{1}{\omega - \omega_A + i\Gamma/2 + i\varepsilon}. \end{aligned} \quad (56)$$

Hence, the time-domain computation previously conducted has simply recovered the poles of the atomic Green function. This confirms that our definitions of ω_A and Γ are fully consistent with the usual approach in scattering theory, in which physical parameters are identified with the poles of the relevant Green function [35, 39], in the present case, the atomic Green function.

Now, we emphasize how this Green function enters the description of single-photon scattering events. The S -matrix always conserves the total energy of the scattering process, and its non-trivial part is contained in the T matrix [27]:

$$S = \mathbb{1} + 2i\pi \delta(E_{\text{out}} - E_{\text{in}}) T. \quad (57)$$

Accordingly, the matrix elements of T are often evaluated *on shell* at a given energy ω and denoted $T(\omega)$. The T operator is formally related to the Green operator $G(\omega)$ through [27]:

$$T(\omega) = V + V G(\omega) V. \quad (58)$$

The numerical data we previously observed were entirely determined, up to the trivial identity contribution, by the matrix elements $T_{\alpha k,g}^{\beta p,g}$. Since the interaction part V does not directly couple $|\alpha k, g\rangle$ to $|\beta p, g\rangle$, the insertion of a complete set of states immediately yields:

$$\begin{aligned} T_{\alpha k,g}^{\beta p,g}(\omega) &= \langle \beta p, g | V | 0, e \rangle \langle 0, e | V | \alpha k, g \rangle \langle 0, e | G(\omega) | 0, e \rangle. \end{aligned} \quad (59)$$

Hence, the physical parameters that determine the amplitudes observed in such scattering events are precisely those encoded in the poles of the atomic Green function $G_{0,e}^{0,e}(\omega) = \langle 0, e | G(\omega) | 0, e \rangle$ that we implicitly manipulated in our time-domain computation. This shows clearly why focusing solely on the decay dynamics of the atom was sufficient to set up our simulation of photon scattering events.

To further analyze the analytic structure of this Green function and its connection to the renormalization relations derived above, one can expand the matrix element in powers of the coupling constant $\gamma^{1/2}$.

B. Perturbative expansion and loop corrections

Diagrammatic representations can be used to visualize perturbative expansions in waveguide QED setups, as in Refs. [28, 35, 46], which correspond to particular cases of Feynman diagrams in quantum field theory [39]. Here, we carefully reformulate these rules for our simplified model, both to investigate the analytic structure of the renormalization relations derived and to ensure a consistent diagrammatic representation for our specific waveguide-QED setup. The T -matrix can be represented as:

$$T_{\alpha k, g}^{\beta p, g} = \begin{array}{c} \text{Diagram: } \text{---} \begin{array}{c} \text{---} \text{---} \\ |g\rangle \quad |g\rangle \end{array} \text{---} \text{---} \end{array} \quad \begin{array}{c} \text{Diagram: } \text{---} \begin{array}{c} \text{---} \text{---} \\ |g\rangle \quad |e\rangle \end{array} \text{---} \begin{array}{c} \text{---} \text{---} \\ |e\rangle \quad |g\rangle \end{array} \text{---} \text{---} \end{array} = \begin{array}{c} \text{Diagram: } \text{---} \begin{array}{c} \text{---} \text{---} \\ |g\rangle \quad |e\rangle \end{array} \text{---} \begin{array}{c} G_e \text{ (circle)} \\ |e\rangle \end{array} \text{---} \begin{array}{c} \text{---} \text{---} \\ |e\rangle \quad |g\rangle \end{array} \text{---} \text{---} \end{array}, \quad (60)$$

where we have shortened the notation $G_{0,e}^{0,e}$ to G_e and adopted the following graphical representations:

$$\langle 0, e | V | \alpha k, g \rangle = i \sqrt{\frac{\gamma}{2}} = \begin{array}{c} \text{Diagram: } \text{---} \begin{array}{c} \text{---} \text{---} \\ |g\rangle \quad |e\rangle \end{array} \text{---} \text{---} \end{array}, \quad (61a)$$

$$\langle \beta p, g | V | 0, e \rangle = -i \sqrt{\frac{\gamma}{2}} = \begin{array}{c} \text{Diagram: } \text{---} \begin{array}{c} \text{---} \text{---} \\ |e\rangle \quad |g\rangle \end{array} \text{---} \text{---} \end{array}, \quad (61b)$$

directly inspired from Refs [28, 35, 46]. On the other hand, starting from the expression of the factor $f(\omega_0, \gamma)$ given in Eq. 46, the following series expansion can be formally written:

$$f(\omega_0, \gamma) = 1 + \sum_{l \geq 1} \gamma^l \left(\frac{1}{\pi H(\omega_0 - \Lambda_{\text{IR}}, \Lambda_{\text{UV}} - \omega_0)} \right)^l. \quad (62)$$

We can now argue that each l -th order partially captures a specific diagrammatic contribution in the poles of the atomic Green function. The Lippmann-Schwinger equation relates the T matrix to the free Green operator [27]:

$$T(\omega) = V + V G_0(\omega) T(\omega), \quad G_0(\omega) = \frac{1}{\omega - H_0 + i\varepsilon}, \quad (63)$$

which makes it possible to express the T matrix as a formal series in powers of the free Green operator:

$$T(\omega) = V + V G_0(\omega) V + V G_0(\omega) V G_0(\omega) V + \dots \quad (64)$$

Using the definition of the full T matrix in Eq. 58, we obtain a corresponding expansion for the full Green op-

erator [27]:

$$G(\omega) = G_0(\omega) + G_0(\omega) V G_0(\omega) + G_0(\omega) V G_0(\omega) V G_0(\omega) + \dots \quad (65)$$

Evaluating the atomic matrix element $\langle 0, e | \cdot | 0, e \rangle$ of this perturbative expansion provides a diagrammatic representation of the atomic Green function in terms of the interaction vertices introduced above. This expansion begins with the tree-level contribution, given by:

$$\langle 0, e | G_0(\omega) | 0, e \rangle = \frac{1}{\omega - \omega_0} \equiv \frac{1}{|e\rangle} \quad (66)$$

which is usually referred to as the *bare atomic propagator* in perturbation theory [39]. The first-order term vanishes identically because $\langle 0, e | V | 0, e \rangle = 0$. The next non-zero contribution is therefore:

$$\begin{aligned} \langle 0, e | G_0(\omega) V G_0(\omega) V G_0(\omega) | 0, e \rangle \\ = \gamma \frac{2\pi}{(\omega - \omega_0)^2} \int \frac{d\omega_1}{2\pi} \frac{1}{\omega - \omega_1}, \end{aligned} \quad (67)$$

which is obtained by two insertions of complete sets of states. This is manifestly divergent when the frequency range is unbounded. This matrix element can be represented diagrammatically as the virtual emission and reabsorption of a photon by the atom [35, 46]:

$$\begin{aligned} \langle 0, e | G_0(\omega) V G_0(\omega) V G_0(\omega) | 0, e \rangle \\ \equiv \begin{array}{c} \text{Diagram: } \text{---} \begin{array}{c} \text{---} \text{---} \\ |e\rangle \quad |g\rangle \end{array} \text{---} \text{---} \end{array} \quad (68) \end{aligned}$$

In standard perturbation theory, one introduces counterterms in the Hamiltonian to render loop diagrams finite order by order [39, 40]. In the present context, however, the situation is quite different. Introducing IR and UV cutoffs directly in numerical simulations makes the loop diagrams finite from the outset, and their effects are instead absorbed into a direct renormalization of the physical parameters. This provides a simple interpretation of the correction we have computed.

Iterating this procedure yields the following expansion of the atomic Green function, which corresponds to the renormalized atomic propagator:

$$G_e(\omega) = \frac{1}{|e\rangle} + \frac{1}{|e\rangle} \text{---} \frac{1}{|g\rangle} \text{---} \frac{1}{|e\rangle} + \frac{1}{|e\rangle} \text{---} \frac{1}{|g\rangle} \text{---} \frac{1}{|e\rangle} \text{---} \frac{1}{|g\rangle} \text{---} \frac{1}{|e\rangle} + \dots \quad (69)$$

Each interaction vertex contributes a factor of $\gamma^{1/2}$ to the corresponding diagram. Conservation of the total number of excitations allows us to anticipate the structure of the expansion: each additional term is generated from the preceding one by inserting an extra loop correction on the atomic line, thereby multiplying the overall amplitude by an additional factor of γ . Hence the expansion may be reorganized as

$$G_e(\omega) = G_0(\omega) + \sum_{l \geq 1} \gamma^l G_e^{(l)}(\omega), \quad (70)$$

where $G_e^{(l)}(\omega)$ denotes the l -loop correction to the atomic Green function. This structure naturally matches the series expansion of $f(\omega_0, \gamma)$ in Eq. 62, and provides a physical interpretation of the effect induced by a narrow frequency window $[\Lambda_{\text{IR}}, \Lambda_{\text{UV}}]$. As the bounds of this frequency window approach each other, the loop corrections of the atomic Green function become progressively resummed, explaining why imposing such bounds naively, without properly accounting for renormalization, leads to inaccurate numerical simulations.

Because our initial time-domain computation is not directly expressed in terms of the diagrammatic expansion, our formula is not expected to reproduce all loop contributions individually. Rather, the argument presented here indicates that our expression captures the *effects* generated by the loop corrections, even though it does not resolve each correction separately. Nonetheless, since the approach is non-perturbative, it succeeds in capturing the full resummation of these contributions, which is precisely what matters for the physical observables.

C. Extension to multi-photon scattering

With the diagrammatic expansion of the S -matrix elements now formally justified, we can employ it to analyze multi-photon scattering processes. In particular, let us consider the T -matrix contribution to the two-photon scattering amplitude $T_{\alpha_1 k_1, \alpha_2 k_2, g}^{\beta_1 p_1, \beta_2 p_2, g}$. The loop corrections contributing to the atomic line arise from the series expansion of the atomic Green's function. Accordingly, the Feynman-diagrammatic expansion of the above amplitude can be recast as:

$$T_{\alpha_1 k_1, \alpha_2 k_2, g}^{\beta_1 p_1, \beta_2 p_2, g} = \text{---} \frac{\alpha_1, k_1}{\text{---}} \text{---} G_e \text{---} \frac{\beta_1, p_1}{\text{---}} \text{---} G_e \text{---} \frac{\beta_2, p_2}{\text{---}} \text{---} \dots + \{\text{perm.}\}, \quad (71)$$

where $\{\text{perm.}\}$ denotes all permutations of the incoming and outgoing photon legs. These permutations correspond precisely to the s -, t -, and u -channel contributions familiar from scattering theory in particle physics [39]. For readability, the subscripts $|g\rangle$ and $|e\rangle$ have been omitted on this diagram. The key point is that the divergences in this amplitude, rendered finite by the introduction of IR and UV cutoffs, are precisely the loop corrections encountered previously.

From a diagrammatic standpoint, this observation can

be extended to multi-photon scattering processes: any corrections capable of renormalizing the physical frequency ω_A or the physical decay rate Γ are identical to those already identified. In particular, the only loop corrections that contribute arise from the atomic Green's function. This restriction is a direct consequence of particle-number conservation within the RWA. Hence, we can safely conclude that the renormalization relations derived in this paper apply generally to multi-photon scattering processes.

VI. CONCLUSION

We presented a non-perturbative derivation of the physical parameters governing light-matter interactions in a waveguide-QED setup, explicitly accounting for the effects of IR and UV cutoffs that are necessarily introduced in numerical simulations. Our approach is based on a first-principles Hamiltonian description and relies on the direct computation of the atomic dynamics in the time domain, which allows us to explicitly track the effects of these cutoffs. We connected our derivation to the standard Green's function formalism in scattering theory, providing a physical interpretation of the renormalization effects in terms of loop corrections, and demonstrated that our results extend naturally to multi-photon scattering processes.

We provided explicit expressions for the physical parameters as functions of the bare ones and the cutoffs, which is of practical importance for the design of accurate and efficient waveguide-QED simulators, since the bare parameters are not directly observable and must be adjusted to reproduce the desired physical behavior. In particular, we introduced a renormalization-aware parameterization that enables physical accuracy to be maintained while reducing the computational cost of simulations by narrowing the effective bandwidth of the model. Although based on a simple model, the end-

to-end, renormalization-aware approach presented in this work paves the way toward the design of resource-efficient light-matter simulators.

Future work could explore extending the present approach to more complex light-matter interaction models, such as multiple TLSs coupled to the same waveguide [27, 35], where virtual photon exchanges between the TLSs may give rise to additional renormalization effects. It would also be interesting to generalize the derivation to a frequency-dependent light-matter coupling $\gamma(\omega)$, thereby accounting for more complex spectral densities [22, 42, 47].

ACKNOWLEDGMENTS

This work was supported by JST Moonshot R&D Program Grant Numbers JPMJMS226C. R.P. acknowledges the hospitality of National Institute of Informatics during the research stay that laid the groundwork for this project.

CODE AVAILABILITY

The code used to produce the numerical results in this work is available at <https://github.com/rpiron/waveguide-qed-simulator>.

-
- [1] E. Knill, R. Laflamme, and G. J. Milburn, A scheme for efficient quantum computation with linear optics, *Nature* **409**, 46 (2001).
- [2] P. Kok, W. J. Munro, K. Nemoto, T. C. Ralph, J. P. Dowling, and G. J. Milburn, Review article: Linear optical quantum computing, *Reviews of Modern Physics* **79**, 135 (2007), arXiv:quant-ph/0512071.
- [3] P. Kok and B. W. Lovett, *Introduction to Optical Quantum Information Processing* (Cambridge University Press, Cambridge, 2010).
- [4] C. H. Bennett, G. Brassard, C. Crépeau, R. Jozsa, A. Peres, and W. K. Wootters, Teleporting an unknown quantum state via dual classical and Einstein-Podolsky-Rosen channels, *Physical Review Letters* **70**, 1895 (1993).
- [5] J. Eisert, K. Jacobs, P. Papadopoulos, and M. B. Plenio, Optimal local implementation of non-local quantum gates, *Physical Review A* **62**, 052317 (2000), arXiv:quant-ph/0005101.
- [6] J. I. Cirac, A. Ekert, S. F. Huelga, and C. Macchiavello, Distributed Quantum Computation over Noisy Channels, *Physical Review A* **59**, 4249 (1999), arXiv:quant-ph/9803017.
- [7] C. Cabrillo, J. I. Cirac, P. Garcia-Fernandez, and P. Zoller, Creation of entangled states of distant atoms by interference, *Physical Review A* **59**, 1025 (1999), arXiv:quant-ph/9810013.
- [8] L.-M. Duan and H. J. Kimble, Efficient engineering of multi-atom entanglement through single-photon detections, *Physical Review Letters* **90**, 253601 (2003), arXiv:quant-ph/0301164.
- [9] S. D. Barrett and P. Kok, Efficient high-fidelity quantum computation using matter qubits and linear optics, *Physical Review A* **71**, 060310 (2005), arXiv:quant-ph/0408040.
- [10] A. Y. Kitaev, Fault-tolerant quantum computation by anyons, *Annals of Physics* **303**, 2 (2003), arXiv:quant-ph/9707021.
- [11] D. Aharonov and M. Ben-Or, Fault-Tolerant Quantum Computation With Constant Error Rate (1999), arXiv:quant-ph/9906129.
- [12] E. Knill, R. Laflamme, and W. H. Zurek, Resilient Quantum Computation: Error Models and Thresholds, *Proceedings of the Royal Society of London. Series A: Mathematical, Physical and Engineering Sciences* **454**, 365 (1998), arXiv:quant-ph/9702058.
- [13] M. O. Scully and M. S. Zubairy, *Quantum Optics* (Cambridge University Press, Cambridge, 1997).
- [14] C. Cohen-Tannoudji, J. Dupont-Roc, and G. Grynberg, *Photons and Atoms: Introduction to Quantum Electrodynamics* (Wiley, 1989).
- [15] E. Jaynes and F. Cummings, Comparison of quantum and semiclassical radiation theories with application to the beam maser, *Proceedings of the IEEE* **51**, 89 (1963).
- [16] J. Larson and T. Mavrogordatos, *The Jaynes-Cummings Model and Its Descendants: Modern Research Directions* (IOP Publishing, 2021).
- [17] M. Havukainen, G. Drobny, S. Stenholm, and V. Buzek, Quantum simulations of optical systems, *Journal of Mod-*

- ern Optics **46**, 1343 (1999), arXiv:quant-ph/9902078.
- [18] J. Oba, S. Kajita, and A. Soeda, Fast simulation for multi-photon, atomic-ensemble quantum model of linear optical systems addressing the curse of dimensionality, *Scientific Reports* **14**, 3208 (2024), arXiv:2302.13953 [quant-ph].
- [19] D. Roy, C. M. Wilson, and O. Firstenberg, Strongly interacting photons in one-dimensional continuum, *Reviews of Modern Physics* **89**, 021001 (2017), arXiv:1603.06590 [quant-ph].
- [20] A. Roulet, H. N. Le, and V. Scarani, Two photons on an atomic beam-splitter: Nonlinear scattering and induced correlations, *Physical Review A* **93**, 033838 (2016), arXiv:1411.6411 [quant-ph].
- [21] Y. S. Greenberg, A. G. Moiseev, and A. A. Shtygashev, Single-photon scattering on a qubit. Space-time structure of the scattered field, *Physical Review A* **107**, 013519 (2023), arXiv:2205.00174 [quant-ph].
- [22] P. Domokos, P. Horak, and H. Ritsch, Quantum description of light pulse scattering on a single atom in waveguides, *Physical Review A* **65**, 033832 (2002), arXiv:quant-ph/0202005.
- [23] J.-T. Shen and S. Fan, Coherent Single Photon Transport in a One-Dimensional Waveguide Coupled with Superconducting Quantum Bits, *Physical Review Letters* **95**, 213001 (2005).
- [24] J.-T. Shen and S. Fan, Strongly-correlated multi-particle transport in one-dimension through a quantum impurity: An outline of exact and complete solutions, *Physical Review A* **76**, 062709 (2007), arXiv:0707.4335 [quant-ph].
- [25] J.-T. Shen and S. Fan, Strongly Correlated Two-Photon Transport in One-Dimensional Waveguide Coupled to A Two-Level System, *Physical Review Letters* **98**, 153003 (2007), arXiv:quant-ph/0701170.
- [26] S. Fan, S. E. Kocabas, and J.-T. Shen, Input-Output Formalism For Few-Photon Transport in One-Dimensional Nanophotonic Waveguides Coupled to a Qubit, *Physical Review A* **82**, 063821 (2010), arXiv:1011.3296 [quant-ph].
- [27] M. Pletyukhov and V. Gritsev, Scattering of massless particles in one-dimensional chiral channel, *New Journal of Physics* **14**, 095028 (2012), arXiv:1203.0451 [quant-ph].
- [28] T. W. Chen, C. K. Law, and P. T. Leung, Propagators of the Jaynes-Cummings model in open systems (2002), arXiv:quant-ph/0201076.
- [29] K. A. Ralley, I. V. Lerner, and I. V. Yurkevich, Hong-Ou-Mandel Interference with a Single Atom, *Scientific Reports* **5**, 13947 (2015), arXiv:1505.03715 [quant-ph].
- [30] T. Shi, D. E. Chang, and J. I. Cirac, Multi-photon Scattering Theory and Generalized Master Equations, *Physical Review A* **92**, 053834 (2015), arXiv:1507.08699 [quant-ph].
- [31] A. Laucht, S. Pütz, T. Günthner, N. Hauke, R. Saive, S. Frédéric, M. Bichler, M.-C. Amann, A. W. Holleitner, M. Kaniber, and J. J. Finley, A Waveguide-Coupled On-Chip Single-Photon Source, *Physical Review X* **2**, 011014 (2012).
- [32] O. Astafiev, A. M. Zagoskin, A. A. Abdumalikov, Y. A. Pashkin, T. Yamamoto, K. Inomata, Y. Nakamura, and J. S. Tsai, Resonance Fluorescence of a Single Artificial Atom, *Science* **327**, 840 (2010), arXiv:1002.4944 [cond-mat].
- [33] D. E. Chang, V. Vuletić, and M. D. Lukin, Quantum nonlinear optics — photon by photon, *Nature Photonics* **8**, 685 (2014).
- [34] D. N. Makarov, Theory for the beam splitter in quantum optics: Quantum entanglement of photons and their statistics, HOM effect (2022), arXiv:2211.03359 [quant-ph].
- [35] A. S. Sheremet, M. I. Petrov, I. V. Iorsh, A. V. Poshakinskiy, and A. N. Poddubny, Waveguide quantum electrodynamics: Collective radiance and photon-photon correlations (2022), arXiv:2103.06824 [quant-ph].
- [36] A. Nysteen, P. T. Kristensen, D. P. S. McCutcheon, P. Kaer, and J. Mørk, Scattering of two photons on a quantum emitter in a one-dimensional waveguide: Exact dynamics and induced correlations, *New Journal of Physics* **17**, 023030 (2015), arXiv:1409.1256 [quant-ph].
- [37] M. Bundgaard-Nielsen, D. Englund, M. Heuck, and S. Krastanov, WaveguideQED.jl: An Efficient Framework for Simulating Non-Markovian Waveguide Quantum Electrodynamics, *Quantum* **9**, 1710 (2025).
- [38] S. Arranz Regidor, G. Crowder, H. Carmichael, and S. Hughes, Modeling quantum light-matter interactions in waveguide QED with retardation, nonlinear interactions, and a time-delayed feedback: Matrix product states versus a space-discretized waveguide model, *Physical Review Research* **3**, 023030 (2021).
- [39] M. E. Peskin and D. V. Schroeder, *An Introduction to Quantum Field Theory* (Addison-Wesley, Reading, USA, 1995).
- [40] J. C. Collins, *Renormalization: An Introduction to Renormalization, the Renormalization Group and the Operator-Product Expansion*, Cambridge Monographs on Mathematical Physics (Cambridge University Press, Cambridge, 1984).
- [41] W. E. Lamb and R. C. Rutherford, Fine Structure of the Hydrogen Atom by a Microwave Method, *Physical Review* **72**, 241 (1947).
- [42] M. Malekakhlagh, A. Petrescu, and H. E. Türeci, Cutoff-free Circuit Quantum Electrodynamics, *Physical Review Letters* **119**, 073601 (2017), arXiv:1701.07935 [quant-ph].
- [43] M. P. Woods, M. Cramer, and M. B. Plenio, Simulating Bosonic Baths with Error Bars, *Physical Review Letters* **115**, 130401 (2015), arXiv:1504.01531 [quant-ph].
- [44] D.-w. Wang, Z.-h. Li, H. Zheng, and S.-y. Zhu, Time evolution, Lamb shift, and emission spectra of spontaneous emission of two identical atoms, *Physical Review A* **81**, 043819 (2010).
- [45] T. F. See, C. Noh, and D. G. Angelakis, Diagrammatic Approach to Multiphoton Scattering, *Physical Review A* **95**, 053845 (2017), arXiv:1702.01632 [quant-ph].
- [46] O. D. Stefano, R. Stassi, L. Garziano, A. F. Kockum, S. Savasta, and F. Nori, Feynman-diagrams approach to the quantum Rabi model for ultrastrong cavity QED: Stimulated emission and reabsorption of virtual particles dressing a physical excitation, *New Journal of Physics* **19**, 053010 (2017).
- [47] C. A. González-Gutiérrez, Non-Markovian dynamics of giant emitters beyond the Weisskopf-Wigner approximation (2025), arXiv:2508.21784 [quant-ph].
- [48] S. Weinberg, *Lectures on Quantum Mechanics*, 2nd ed. (Cambridge University Press, Cambridge, 2015).

Supplementary Material

Appendix A: Derivation of the Runge-Kutta scheme

We provide the full derivation of the equations used to estimate the system's state within the fourth-order Runge-Kutta scheme. Assume that the total simulation time T and the number of steps N_{steps} are fixed. We then define the discretization time step as

$$\delta t = \frac{T}{N_{\text{steps}}}. \quad (\text{A1})$$

The interaction time window is discretized into time slices $t_n = n \delta t$, and the state is propagated according to the following scheme [17]:

$$|\psi(t_{n+1} = t_n + \delta t)\rangle = |\psi(t_n)\rangle + \frac{1}{6} (|\psi_{n,1}\rangle + 2|\psi_{n,2}\rangle + 2|\psi_{n,3}\rangle + |\psi_{n,4}\rangle), \quad (\text{A2})$$

where the intermediate states involved in this sum are defined as follows:

$$|\psi_{n,1}\rangle = -i\delta t V_I(t_n) |\psi(t_n)\rangle, \quad (\text{A3a})$$

$$|\psi_{n,2}\rangle = -i\delta t V_I\left(t_n + \frac{\delta t}{2}\right) \left(|\psi(t_n)\rangle + \frac{1}{2} |\psi_{n,1}\rangle \right), \quad (\text{A3b})$$

$$|\psi_{n,3}\rangle = -i\delta t V_I\left(t_n + \frac{\delta t}{2}\right) \left(|\psi(t_n)\rangle + \frac{1}{2} |\psi_{n,2}\rangle \right), \quad (\text{A3c})$$

$$|\psi_{n,4}\rangle = -i\delta t V_I(t_n + \delta t) \left(|\psi(t_n)\rangle + \frac{1}{2} |\psi_{n,3}\rangle \right). \quad (\text{A3d})$$

Since the particle number N is conserved, the ability to efficiently compute the action of $V_I(t)$ on an N -particle state enables an efficient implementation of the scheme. We present the explicit relations in the $N = 1$ sector (single-excitation regime), which are used for the single-photon scattering simulations. A single-particle state can be written as:

$$|\psi\rangle = \sum_{\alpha,k} c_{\alpha k} |\alpha k, g\rangle + b |0, e\rangle, \quad (\text{A4})$$

Let us denote N_{modes} the number of modes retained after introducing the IR and UV cutoffs Λ_{IR} and Λ_{UV} . The single particle state is numerically represented as:

$$|\psi\rangle = \begin{pmatrix} c_{1k} \\ c_{2k} \\ b \end{pmatrix} \equiv \begin{pmatrix} c_\nu \\ b \end{pmatrix}, \quad (\text{A5})$$

where the indices α and k are grouped into a single index $\nu = 1, \dots, 2N_{\text{modes}}$, which runs over two copies of the photonic modes corresponding to the two propagation channels. The dimension of the numerical Hilbert space introduced in the main text is expressed in terms of the number of modes as:

$$\dim(\mathcal{H}_{\text{num}}) = 2N_{\text{modes}} + 1. \quad (\text{A6})$$

Recall from the main text the Hamiltonian in the interaction picture:

$$V_I(t) = i\sqrt{\frac{\gamma}{2L}} \sum_{\alpha,k} \left[e^{-i(\omega_k - \omega_0)t} a_{\alpha k} \sigma^+ - \text{h.c.} \right], \quad (\text{A7})$$

which acts on the eigenbasis of H_0 , restricted to the single-excitation subspace as [17]:

$$V_I(t) |\alpha k, g\rangle = i\sqrt{\frac{\gamma}{2L}} e^{-i(\omega_k - \omega_0)t} |0, e\rangle, \quad (\text{A8a})$$

$$V_I(t) |0, e\rangle = -i\sqrt{\frac{\gamma}{2L}} \sum_{\alpha,k} e^{i(\omega_k - \omega_0)t} |\alpha k, g\rangle. \quad (\text{A8b})$$

By defining the vector:

$$V_\nu(t) = -i\sqrt{\frac{\gamma}{2L}} \begin{pmatrix} e^{i(\omega_k - \omega_0)t} \\ e^{i(\omega_k - \omega_0)t} \end{pmatrix}, \quad (\text{A9})$$

the update rule can be written compactly as

$$V_I(t) |\psi\rangle = \begin{pmatrix} b V_\nu(t) \\ \mathbf{V}(t)^\dagger \mathbf{c} \end{pmatrix}, \quad (\text{A10})$$

where we introduced the shorthand notation for the scalar product

$$\mathbf{V}(t)^\dagger \mathbf{c} = \sum_\nu V_\nu^*(t) c_\nu. \quad (\text{A11})$$

Hence, applying the Hamiltonian to a single state incurs a computational cost of $\mathcal{O}(\dim(\mathcal{H}_{\text{num}}))$, rather than $\mathcal{O}(\dim(\mathcal{H}_{\text{num}})^2)$, which would result from a naive matrix multiplication that does not exploit the sparse structure of the Hamiltonian. This update rule enables the successive construction of the intermediate states $|\psi_{n,i}\rangle$ from $|\psi(t_n)\rangle$, and ultimately the evaluation of $|\psi(t_{n+1})\rangle$ with an overall computational cost scaling as $\mathcal{O}(N_{\text{modes}})$.

Appendix B: Explicit computation of Taylor's expansion coefficients

In this appendix, we derive explicit expressions for the coefficients α_0 and α_1 :

$$\alpha_0 = -\frac{\gamma}{2} + i\frac{\gamma}{2\pi} \log\left(\frac{\Lambda_{\text{UV}} - \omega_0}{\omega_0 - \Lambda_{\text{IR}}}\right), \quad (\text{B1a})$$

$$\alpha_1 = -\frac{\gamma}{2\pi} \left(\frac{1}{\Lambda_{\text{IR}} - \omega_0} - \frac{1}{\Lambda_{\text{UV}} - \omega_0} \right), \quad (\text{B1b})$$

and we also comment on the scaling of the higher-order coefficients α_n with the bandwidth for $n \geq 2$. Let us first start from the definition of α_0 in the presence of frequency bounds:

$$\alpha_0 = -\frac{\gamma}{2\pi} \int_0^\infty \int_{\Lambda_{\text{IR}}}^{\Lambda_{\text{UV}}} e^{-i(\omega - \omega_0)\tau} d\omega d\tau, \quad (\text{B2})$$

Now, switching the order of integration and using the integral formula valid for any real number x :

$$\int_0^\infty e^{\pm ix\tau} d\tau = \pi\delta(x) \pm i\mathcal{P}\left(\frac{1}{x}\right), \quad (\text{B3})$$

where $\mathcal{P}(.)$ is the principal value, one obtains:

$$\begin{aligned} \alpha_0 &= -\frac{\gamma}{2\pi} \int_{\Lambda_{\text{IR}}}^{\Lambda_{\text{UV}}} d\omega \left[\pi\delta(\omega - \omega_0) - i\mathcal{P}\left(\frac{1}{\omega - \omega_0}\right) \right] \\ &= -\frac{\gamma}{2} + i\frac{\gamma}{2\pi} \text{V.p} \left(\int_{\Lambda_{\text{IR}}}^{\Lambda_{\text{UV}}} \frac{d\omega}{\omega - \omega_0} \right), \end{aligned} \quad (\text{B4})$$

where we recall the definition of the Cauchy's principal value:

$$\text{V.p} \left(\int_{\Lambda_{\text{IR}}}^{\Lambda_{\text{UV}}} \frac{d\omega}{\omega - \omega_0} \right) = \lim_{\epsilon \rightarrow 0^+} \left(\int_{\Lambda_{\text{IR}}}^{\omega_0 - \epsilon} \frac{d\omega}{\omega - \omega_0} + \int_{\omega_0 + \epsilon}^{\Lambda_{\text{UV}}} \frac{d\omega}{\omega - \omega_0} \right) \quad (\text{B5})$$

Hence:

$$\alpha_0 = -\frac{\gamma}{2} + i\frac{\gamma}{2\pi} \log\left(\frac{\Lambda_{\text{UV}} - \omega_0}{\omega_0 - \Lambda_{\text{IR}}}\right) \quad (\text{B6})$$

As for α_1 , from the main text:

$$\alpha_1 = \frac{\gamma}{2\pi} \int_0^\infty d\tau \int_{\Lambda_{\text{IR}}}^{\Lambda_{\text{UV}}} d\omega \tau e^{-i(\omega - \omega_0)\tau}. \quad (\text{B7})$$

The idea is, similarly to the treatment of α_0 , to interchange the order of integration between time and frequency. This is justified by the following integral identity:

$$\int_0^\infty \tau e^{\pm ix\tau} d\tau = \mp i\pi \delta^{(1)}(x) - \mathcal{P}\left(\frac{1}{x^2}\right), \quad (\text{B8})$$

but a few comments are in order regarding the first term. The distribution $\delta^{(1)}(x)$ should be understood as the derivative of the Dirac delta in the sense of distributions. That is, for any test function $\phi(x)$,

$$\int dx \phi(x) \delta^{(1)}(x) = - \int dx \phi'(x) \delta(x). \quad (\text{B9})$$

With this point clarified, we can now proceed with the computation:

$$\begin{aligned} \alpha_1 &= \frac{\gamma}{2\pi} \int_{\Lambda_{\text{IR}}}^{\Lambda_{\text{UV}}} d\omega \left[i\pi \delta^{(1)}(\omega - \omega_0) - \mathcal{P}\left(\frac{1}{(\omega - \omega_0)^2}\right) \right] \\ &= i\frac{\gamma}{2} \underbrace{\int_{\Lambda_{\text{IR}}}^{\Lambda_{\text{UV}}} d\omega \delta^{(1)}(\omega - \omega_0)}_{=0} - \frac{\gamma}{2\pi} \text{V.p.} \left(\int_{\Lambda_{\text{IR}}}^{\Lambda_{\text{UV}}} \frac{d\omega}{(\omega - \omega_0)^2} \right). \end{aligned} \quad (\text{B10})$$

Collecting the remaining contribution, one obtains:

$$\alpha_1 = -\frac{\gamma}{2\pi} \left(\frac{1}{\Lambda_{\text{IR}} - \omega_0} - \frac{1}{\Lambda_{\text{UV}} - \omega_0} \right). \quad (\text{B11})$$

The final aspect to discuss is the scaling behavior stated in the main text:

$$\alpha_n = x_n \frac{\gamma}{(\omega_0 - \Lambda_{\text{IR}})^n} + y_n \frac{\gamma}{(\Lambda_{\text{UV}} - \omega_0)^n}, \quad n \geq 1, \quad (\text{B12})$$

Starting from the definition:

$$\alpha_n = \frac{(-1)^{n+1}}{n!} \frac{\gamma}{2\pi} \int_0^\infty d\tau \int_{\Lambda_{\text{IR}}}^{\Lambda_{\text{UV}}} d\omega \tau^n e^{-i(\omega - \omega_0)\tau}, \quad (\text{B13})$$

one can verify the recursive relation:

$$\alpha_{n+1} = \frac{i}{n+1} \frac{d\alpha_n}{d\omega_0}, \quad (\text{B14})$$

which is consistent with the explicit expressions of α_0 and α_1 derived above, providing a useful sanity check. Iterating from α_1 yields:

$$\begin{aligned} \alpha_n &= \frac{i^{n-1}}{n!} \frac{d^{n-1} \alpha_1}{d\omega_0^{n-1}} \\ &= -\frac{i^{n-1} \gamma}{2n! \pi} \left(\frac{d^{n-1}}{d\omega_0^{n-1}} (\Lambda_{\text{IR}} - \omega_0)^{-1} - \frac{d^{n-1}}{d\omega_0^{n-1}} (\Lambda_{\text{UV}} - \omega_0)^{-1} \right), \end{aligned} \quad (\text{B15})$$

which exactly reproduces the scaling form of Eq. B12.